

# Modelling and Validation of Contributions to Stress in the Shallow Trench Isolation Process Sequence

K. Garikipati<sup>1</sup>, V.S. Rao<sup>2</sup>, M.Y. Hao<sup>3</sup>, E. Ibok<sup>4</sup>, I. de Wolf<sup>5</sup>, R. W. Dutton<sup>6</sup>

**Abstract:** This work is based upon a careful rendering of mechanics and mathematics to describe the phenomena that influence the stress engendered by the Shallow Trench Isolation process. The diffusion-reaction problem is posed in terms of fundamental mass balance laws. Finite strain kinematics is invoked to model the large expansion of SiO<sub>2</sub>, dielectrics are modelled as viscoelastic solids and annealing-induced density relaxation of SiO<sub>2</sub> is incorporated as a history-dependent process. A levelset framework is used to describe the moving Si/SiO<sub>2</sub> interface. Sophisticated finite element methods are employed to solve the mathematical equations posed for each phenomenon. These include the incorporation of discontinuity-resolving shape functions to describe jumps in concentration of O<sub>2</sub>, methods to prevent oscillations of numerical solutions and techniques that allow highly inhomogeneous deformation of a single element. The use of experimental data to rigorously obtain material properties is emphasized. Mechanical properties of viscoelastic solids are extracted directly from stress-strain data, following which, parameters for the diffusion-reaction problem are obtained. Qualitative and quantitative validation of the models is presented; the latter by comparison with micro-Raman spectroscopy measurements.

**keyword:** mechanics, diffusion, reaction, coupled, finite elements

## 1 Introduction

Shallow Trench Isolation (STI) has increasingly displaced Local Oxidation of Silicon (LOCOS) and its variants as the isolation technology of choice for manufacture of integrated circuits. Future generations of devices are likely to witness a greatly increased use of STI technology. The main advantage of STI over LOCOS lies in its scalability. A drawback lies in the fact that process steps such as etching, thermal oxidation, deposition and densification of gap-fill materials and rapid thermal annealing contribute in large or small measure to the creation and alteration of stress in the structure. Sufficiently high stresses can lead to the generation of dislocations in the substrate, in turn resulting in deleterious electrical ef-

fects such as leakage currents or electrical shorting between elements [Fahey, Mader, Stiffler, Mohler, Mis, and Slinkman (1992)]. Even in the absence of dislocations, the strains associated with certain stress fields lead to higher leakage currents [Smeys, Griffin, Rek, deWolf, and Saraswat (1999)]. Finally, the failure to achieve sufficient rounding of the substrate at the trench's top corner - a feature reflecting the influence of stress on oxidation - has been related to corner leakage currents [Chang et al. (1997)]. There is clearly a need for accurate modelling of stress. In order to provide a background for this work, we begin with a review of earlier investigations into the stress induced during processing of silicon.

The pioneering work of EerNisse (1979) established the fact that stress is generated during the thermal oxidation of Silicon. It was also recognized that the mechanical response changes character with temperature; thermal growth over 1000°C results in low or vanishing stress. The stress is compressive in nature and is caused by the fact that the molar volume of newly formed SiO<sub>2</sub> is 2.2× that of Silicon. When constrained by a substrate and, possibly constrained by older SiO<sub>2</sub> or other materials, this newly formed SiO<sub>2</sub> is unable to expand to its natural volume and develops compressive stress. Pilling and Bedworth (1923) explained the stress in terms of the shear strain created in the SiO<sub>2</sub>. Vermilyea (1957) extended the notion of a "kink site" (proposed by Mott) to model the expansion of SiO<sub>2</sub>. According to this model, the oxide expands in a one-dimensional manner; i.e., perpendicular to the surface being oxidized. This feature has been incorporated into most studies of the problem up to this point.

Early attempts to model the mechanics of SiO<sub>2</sub> were made by Chin (1983) who adopted a viscous model with constant viscosity. A linear elastic model was used by Hsueh and Evans (1983) and an "incrementally" linear elastic model by Needs, Jovic, Taylor, Board, and Cooke (1986). A nonlinear viscous model was proposed by Rafferty (1989), based on the Eyring-viscous model [Eyring (1936)]. Hsueh and Evans (1983) carried out analytic calculations on oxidation of cylinders using a linear Maxwell-viscoelastic model and Rafferty (1989) extended it to a nonlinear viscoelastic model by replacing the constant viscosity with Eyring's nonlinear viscous model. This model has subsequently been used by many researchers; Hu (1991); Fahey, Mader, Stiffler, Mohler, Mis, and Slinkman (1992); Uchida, Fujinaga, Kotani, Kawazu, and Miyoshi (1996); Senz, Collard, Ferreira, and Baccus (1996)

<sup>1</sup> Stanford University, Stanford, California

<sup>2</sup> Schlumberger Cambridge Research Centre, Cambridge, UK

<sup>3</sup> Advanced Micro Devices Inc., Santa Clara, California

<sup>4</sup> Advanced Micro Devices Inc., Santa Clara, California

<sup>5</sup> Interuniversity Micro-electronics Center, Leuven, Belgium

<sup>6</sup> Stanford University, Stanford, California

to name a few. Navi and Dunham (1997) modelled the oxide as a viscous, compressible fluid. The nonlinear (Eyring) viscous model used in many of the above investigations was introduced to mitigate the artificially high stress calculated using a linear viscosity. It includes a threshold stress above which the viscosity decays exponentially. More recently, Yu, Flinn, and Bravman (1996) adopted a viscosity increasing linearly with time in a Maxwell-viscoelastic model to fit stress-relaxation data for thin oxide films. The stress levels observed in the thin film experiments were too low to activate the decaying character of calibrated Eyring viscosity models.

The above body of work is based on the infinitesimal strain theory of mechanics, which holds for strains up to 5%. It is a fundamental result of the mechanics of deformable bodies that, beyond this range, the infinitesimal strain theory is inaccurate. It fails to account for rotations and nonlinearities inherent in the material behavior. For  $\text{SiO}_2$ , an expansion ratio of  $2.2 \times$  over Silicon, implies strains of the order of  $2.2^{1/3} - 1$  (as pointed out by Hu (1991)); thus casting the problem clearly outside the realm of the infinitesimal strain theory. The interested reader is directed to classical works by Green and Zerna (1954); Truesdell and Noll (1965); Malvern (1969); Chadwick (1976); Gurtin (1981); Marsden and Hughes (1994); Ogden (1984) among others that discuss the finite strain theory of mechanics.

The one-dimensional expansion of newly formed  $\text{SiO}_2$  fails to model the experimentally observed curvature of wafers that have thermal oxide grown on one surface. This aspect of thermal oxidation, which, in fact, formed the experimental basis of EerNisse's pioneering study [EerNisse (1979)], appears to have been largely ignored in the models which followed. While thermal oxidation of planar wafers at temperatures above  $1000^\circ\text{C}$  results in low or nearly zero stress, there exists, to the authors' knowledge, little convincing evidence to suggest that this is on account of one-dimensional oxide expansion. Rather, the reason is to be sought in the rapid viscous (or viscoelastic) stress relaxation. More recently, Yu and co-workers [Yu, Flinn, and Bravman (1997)] have reported the curvature of wafers during thermal growth of  $\text{SiO}_2$  on one surface. A three-dimensional expansion of  $\text{SiO}_2$  is necessary to explain these results. It has been well established in the study of thin films that the tendency for in-plane expansion of the film (in this case,  $\text{SiO}_2$ ) causes curvature of the wafer away from the film. This effect is exploited by way of Stoney's formula [Stoney (1909)] for the purpose of measuring thin film mechanical properties.

The various viscous and viscoelastic models adopted in the above works suffer from a common drawback: they necessarily model a fluid, not a solid. This fact has been pointed out by Hu (1991) and poses the following difficulty: In a structure with oxide that has ceased to flow, the model predicts no stress. Non-zero stresses are approximated by resorting to ad hoc models such as the time-dependent viscosity of Yu,

Flinn, and Bravman (1996, 1997) or by reporting the stress that existed just before the flow ceased as in TSUPREM-4 (1996). Experiments such as those by Yu, Flinn and Bravman (reproduced here in Fig. 3 and 4) demonstrate that the oxide stress does indeed tend asymptotically to a non zero value at temperatures below  $900^\circ\text{C}$ . From Stoney's equation it follows that the wafer curvature is constant when the stress becomes constant; i.e., there is no flow. Without flow, any Maxwell-viscoelastic model (with linear or nonlinear viscosity) calculates zero stress. There is a need for a model that can span the range from fluid-like (stress depends on strain rate) to solid-like (stress depends on strain and, possibly, strain rate) behavior.

There are two origins of stress in the STI process in addition to the expansion of thermal oxide: (i) Volume change of filler materials (usually, TEOS) during densification and subsequent thermal annealing and (ii) unequal coefficients of thermal expansion between dissimilar materials. A film, on being deposited undergoes shrinkage or expansion as a result of the associated chemical reactions. This process leads to stress when the deposited film is bonded to a substrate or fills a trench. Stademüeller (1992) has studied mechanisms of stress generation due to densification of various CVD films. The proper modelling of this effect is crucial to calculations of the stress associated with the STI process since relatively large amounts of deposited trench-fill materials are used. When  $\text{SiO}_2$  is annealed at temperatures at or higher than  $950^\circ\text{C}$ , a relaxation is observed in its density. This phenomenon has been investigated by Irene, Tierney, and Angilello (1982), who modelled it on the basis of a Maxwell-viscoelastic solid. Later, Taniguchi, Tanaka, and Hamaguchi (1990) provided a phenomenological treatment, wherein the relaxation is modelled parametrized by temperature. Since this density relaxation implies a gradual expansion of oxide (beyond the initial  $2.2 \times$  increase over Silicon), it too must be accounted for while modelling the stress. Indeed, for large annealing times, this process results in a volume increase of 3-4% at temperatures above  $1000^\circ\text{C}$ . The importance of modelling the thermal mismatch stress should be apparent since the process involves dissimilar materials and a range of temperatures (for instance, while oxidation occurs at temperatures over  $1000^\circ\text{C}$ , deposition takes place around  $700^\circ\text{C}$  and etching at around  $50^\circ\text{C}$ ). The temperature at which each material is free of thermal strain must be determined and accounted for to enable the correct calculation of stress due to this effect.

Apart from the actual modelling of the mechanics, there are important issues dealing with determination of material parameters. Traditionally, this has been carried out by calibration of computer code; i.e., adjustment of parameters to match geometrical data such as thickness of oxide grown. A benchmark for this type of calibration is the work of Kao (1986) on growth of oxide on cylinders and in holes. Admittedly, this approach is valid for parameters directly related to growth such

as stress-free diffusivity and reaction rate, or the activation volumes for diffusion and reaction. Typically however, this has been extended to parameters in the mechanical model such as the viscosity and, in the case of stress-dependent viscosity, to the corresponding activation volume. This approach was followed by Rafferty (1989); Senez, Collard, Ferreira, and Baccus (1996) and others. Smeys, Griffin, and Saraswat (1995) used an approximate integration of the Maxwell-viscoelastic model to estimate the viscosity of nitride by comparison with micro-Raman stress measurements. With this value fixed, the remaining parameters were calibrated in the above manner. The objection to this approach is that no direct measurement of the stress is involved in extracting the mechanical parameters. It seems artificial that a mechanical parameter like the viscosity should be chosen by fitting growth data. Furthermore, a number of parameter sets could potentially fit the same data. These pitfalls were demonstrated by Smeys, Griffin, and Saraswat (1995).

The stress-free diffusivity and reaction rate are calculated from the Deal-Grove parameters [Deal and Grove (1965)] which, in turn are established for planar oxidation. The assumption involved here is that planar oxidation does not create intrinsic oxide growth stresses. As observed by EerNisse (1979); Yu, Flinn, and Bravman (1997), this assumption is fallacious. This aspect has been alluded to earlier in this section. The values extracted on the basis of planar oxidation are, in fact, the diffusivity and reaction rate corresponding to the stress created by planar oxidation. It follows that the true stress-free diffusivity and reaction rate must also be recalculated.

While early investigations into the mechanics associated with integrated circuits adopted analytic methods, the trend toward numerical analysis has been growing [see Dutton (1983); Rafferty (1989); Peng, Chidambarrao, and Srinivasan (1991); Senez, Collard, Ferreira, and Baccus (1996); Uchida, Fujinaga, Kotani, Kawazu, and Miyoshi (1996); Cea and Law (1996); Rueda, Cea, and Law (1997)] and references therein). Increasingly, the Finite Element Method has been the spatial discretization technique of choice. The relevance of the above investigations to modelling of the STI process lies in their treatment of thermal oxidation of Silicon. The relevant mathematical models are solved as follows: The diffusion of  $O_2$  through an existing layer of  $SiO_2$  is solved. The free surface boundary condition is specified in terms of solubility of the oxidant. The  $SiO_2/Si$  interface is also treated as a boundary across which the oxidant flux vanishes. The  $O_2$  diffusing through to the interface reacts to form  $SiO_2$  causing the boundary to advance further into Si. In a finite element setting, this problem has been treated by specifying an element to be either  $SiO_2$  or Si. This introduces a set of element edges that conform to the interface in its initial position. The interface velocity is calculated from the flux and definition of the interface is updated after each time step. This procedure leads to two difficulties from a computational standpoint: (i) The finite element

mesh must be updated after each timestep to redefine  $SiO_2$  and Si regions - at high computational cost. (ii) The necessity of having element edges that conform to the interface can result in poor mesh quality as the problem progresses. With the  $SiO_2$  and Si regions of the mesh redefined after the solution of the diffusion equation, the equation of mechanical equilibrium is solved for the stresses engendered by the expanding oxide. In cases where the oxide has been treated as an incompressible material (e.g. TSUPREM-4 (1996)) finite element methods have been employed that accurately treat the incompressible limit of deformable bodies.

Following the above review of the field, the present study is outlined: The mathematical and numerical formulation upon which this work is based were developed by Rao and Hughes (1999); Rao, Hughes, and Garikipati (1999). Enhancements and refinements in the mechanics and computational methods (to appear in a separate publication) have been introduced over this original work. The details of the formulations will be avoided for the sake of brevity. The interested reader is directed to the works appearing at the beginning of this paragraph. Sec. 2 discusses the mathematical and numerical formulations. Extraction of material parameters is dealt with in Sec. 3. Validation, qualitative and quantitative, is presented in Sec. 4, and Sec. 5 summarizes the paper with indications of current and future investigations.

## 2 Mathematical and numerical formulations

This section describes the mathematical and numerical models for physical phenomena associated with the STI process. The mathematical models are discussed first. Since thermal oxidation is an important component of the STI process, and has been discussed extensively in the literature, the development begins with this aspect and proceeds to others, more specific to shallow trench isolation.

### 2.1 Mathematical models

Thermal oxidation of Silicon is carried out by introducing the substrate in a dry or wet ambient of  $O_2$  at temperatures ranging between  $800^\circ C$  and  $1200^\circ C$ . The oxidant dissolves in the substrate and reacts with Si forming  $SiO_2$ . Thereafter, for the reaction to proceed, the oxidant must diffuse through the  $SiO_2$  to reach the Si/ $SiO_2$  interface. The reaction at the interface yields newly formed  $SiO_2$ ; thereby the interface advances into the Si. The newly formed  $SiO_2$  has a molar volume  $2.2\times$  that of Si when unstressed; however, it is constrained by the surrounding Si and  $SiO_2$  resulting in the development of stresses in the structure.

#### 2.1.1 Diffusion-reaction

Diffusion and reaction can be combined in the following framework: Consider an observer who has no means of detecting the fact that reactions are taking place. To such an observer

the oxidizing species diffuses through SiO<sub>2</sub> and arrives at the interface which itself is moving at a certain velocity. The flux of O<sub>2</sub> has a discontinuity at the interface; it may either vanish or decrease significantly. Such a setting is appropriate for the application of generalized mass balance laws. Denoting the flux of SiO<sub>2</sub> by  $\mathbf{T}_{\text{OX}}$ , its concentration by  $\rho_{\text{OX}}$  and the normal to the interface pointing into Si by  $\mathbf{n}$ , Rao and Hughes (1999) have shown that the normal velocity of the interface into the Silicon is given by

$$V_n = - \frac{[[\mathbf{T}_{\text{OX}} \cdot \mathbf{n}]]}{[[\rho_{\text{OX}}]]}. \quad (1)$$

In the above equation,  $[[\cdot]]$  denotes the discontinuity in the argument. Eq. 1 is a version of the well-known Rankine-Hugoniot relationship which makes its appearance in classical compressible fluid mechanics in the presence of shocks; i.e., discontinuities in field quantities [see LeVeque (1992) for details].

The chemical reaction of oxidation at equilibrium is written as:



Using the notation  $[\text{SiO}_2]$  to denote the rate of formation of SiO<sub>2</sub> per unit interface area; i.e., a flux, chemical kinetics can be invoked at equilibrium to write

$$[\text{SiO}_2] = k_s \rho_i, \quad (3)$$

where,  $\rho_i$  is the O<sub>2</sub> concentration on the SiO<sub>2</sub> side of the interface. Observing that in Eq.3 and 1,  $-[\text{SiO}_2]$  and  $[[\mathbf{T}_{\text{OX}} \cdot \mathbf{n}]]$  respectively denote the same quantity; namely, the discontinuity in flux of SiO<sub>2</sub>, these equations are combined to give:

$$V_n = \frac{k_s \rho_i}{[[\rho_{\text{OX}}]]}. \quad (4)$$

Now,  $[[\rho_{\text{OX}}]] = \rho_{\text{OX}}^+ - \rho_{\text{OX}}^-$ , where the superscripts  $(\cdot)^+$  and  $(\cdot)^-$  denote the argument evaluated at the interface approached from the Si and SiO<sub>2</sub> regions respectively. Furthermore since  $\rho_{\text{OX}}^+$  is negligible in comparison with  $\rho_{\text{OX}}^-$ , we have, using the common notation  $N_1$  for  $\rho^-$ ,

$$V_n = - \frac{k_s \rho_i}{N_1}. \quad (5)$$

This completes our mathematical formulation of the chemical kinetics of oxidation. The reaction constant  $k_s$  is stress and temperature-dependent. The particular form adopted for the stress dependence will be discussed in Sec. 2.1.5

For the diffusion equation, assuming steady state conditions, and recognizing the absence of sources, the differential equation to be solved is,

$$\nabla \cdot (D \nabla \rho) = 0, \quad (6)$$

where,  $D$  is the diffusivity,  $\nabla$  is the gradient operator and  $\nabla \cdot$  is the divergence operator. Note that in Eq. 6 the diffusing species is O<sub>2</sub>. In general,  $D$  is stress and temperature-dependent. The stress dependence is discussed at the end of Sec. 2.1.5. The diffusion equation is to be solved over SiO<sub>2</sub> and Si domains. Appropriate boundary conditions must be specified in terms of concentration or flux. Flux and concentration discontinuities are to be enforced at the interface.

### 2.1.2 Moving interface: level-set method

The above mathematical formulation of the diffusion-reaction problem provides an expression, i.e., Eq. 5 for the interface velocity. This velocity can be incorporated into a partial differential equation dictating the evolution of the interface by adopting the levelset formulation of Sethian (1996).

A scalar function  $\phi(\mathbf{x}, t)$  is introduced on the domain of interest. The spatial position of the point in question is denoted  $\mathbf{x}$  and the current time is  $t$ . The function  $\phi(\mathbf{x}, t)$  is defined as the signed minimum distance of any point from the interface. Thus, points lying in the Si substrate have  $\phi < 0$ , those on the interface have  $\phi = 0$  and all others have  $\phi > 0$ . Observe that the function so introduced is a purely mathematical entity and does not represent a quantity occurring in a physical process. As the diffusion-reaction processes evolve  $\phi$  changes with position and time. Beginning with the total time derivative of  $\phi(\mathbf{x}, t)$  the following equation can be derived:

$$\frac{d\phi}{dt} = \frac{\partial \phi}{\partial t} - V_n \|\nabla \phi\| = 0. \quad (7)$$

As in Sec. 2.1.1,  $V_n$  is the normal velocity of the interface,  $\nabla \phi$  is the gradient of  $\phi$ ; i.e., a vector, and,  $\|\cdot\|$  denotes the magnitude of a vector. Eq. 7 is a nonlinear partial differential equation. It is sometimes called as the Hamilton-Jacobi equation and, in the context of advective flows would be referred to as a nonlinear advection equation. It is a hyperbolic differential equation and its solution requires the specification of an initial condition; i.e.,

$$\phi(\mathbf{x}, 0) = \phi_0(\mathbf{x}). \quad (8)$$

### 2.1.3 Mechanics

The finite strain formulation which underlies the description of the mechanics in this work will now be outlined. The motivation for this setting is as follows: Each molecule of SiO<sub>2</sub>, on being formed at the interface expands to a stress-free volume that is 2.2× that of the consumed Si molecule. Accordingly, every point in the SiO<sub>2</sub> has a stress-free volumetric strain of 120% when compared with its undeformed state. Even under a stress, the volumetric strain is expected to be very large. As mentioned earlier in this work, it is well known that the infinitesimal formulation of mechanics loses mathematical and physical validity beyond about 5% strain. Furthermore, with finite rotations but no deformation of the material, this theory

results in spurious non-zero stresses. The mechanics of the oxidation problem thus place it well outside the regime of the infinitesimal strain theory, and, the finite strain theory of mechanics must be applied.

Every material point is described by its position  $\mathbf{X}$ , in the undeformed state, relative to a fixed cartesian reference frame. Under a deformation the point's new position,  $\mathbf{x}$ , is given by

$$\mathbf{x} = \mathbf{X} + \mathbf{u}(\mathbf{X}), \quad (9)$$

where,  $\mathbf{u}$  is the displacement vector. The current position is also denoted  $\varphi(\mathbf{X}) = \mathbf{X} + \mathbf{u}(\mathbf{X})$ . The fundamental measure of strain is now introduced:

$$\mathbf{F} = \frac{\partial \mathbf{x}}{\partial \mathbf{X}}, \quad (10)$$

where,  $\mathbf{F}$  is termed the deformation gradient. Additional measures of strain can be introduced, such as,

$$\mathbf{C} = \mathbf{F}^T \mathbf{F}, \quad (11)$$

where,  $\mathbf{C}$  is called the Right Cauchy-Green tensor. Note that this newly introduced strain is nonlinearly dependent upon the displacement  $\mathbf{u}$ . The volumetric expansion ratio is given by

$$J = \det(\mathbf{F}) = \sqrt{\det(\mathbf{C})}, \quad (12)$$

where,  $J$  is called the jacobian of the deformation and must remain positive.

The constitutive law that determines the stress developed in viscoelastic materials is introduced now. The Standard Solid Viscoelastic model [Simo (1985)] was adopted for the oxide. A schematic representation of the model in terms of springs and viscous dashpots in the one dimensional case appears in Fig. 1.

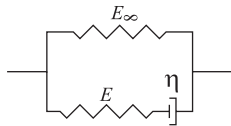


**Figure 1** : Schematic representation of the standard solid viscoelastic model for the one dimensional case

This model also makes an appearance in the literature under the name of the ‘‘Poynting-Thomson Model’’ [Rekhson (1986)]. For the model depicted in Fig. 1, it can be shown that the one-dimensional stress-strain law is given by

$$\sigma(t) = \int_{s=0}^{s=t} \left( E_{\infty} + E \exp\left[\frac{-(t-s)}{\tau}\right] \right) \dot{\epsilon}(s) ds, \quad (13)$$

where,  $\tau = \eta/E$  is a relaxation time. The springs and dashpots appearing in Fig. 1 are, in the three dimensional case, generalized to elastic moduli and viscous relaxation laws for

the stress. These parameters can be extracted from experimental data (see Sec. 3 for details). Higher order models are obtained by adding Maxwell elements (i.e., a spring and dashpot in series, in the above representation). This model has the desirable characteristic of being able to span the entire range of rate-dependent behaviour from a purely viscous fluid, through a Maxwell Viscoelastic Fluid to a Viscoelastic Solid. Thereby, the tendency of the oxide to flow more freely at higher temperatures can be well represented. The Standard Solid Viscoelastic model has also been applied to Silicon Nitride for this work.

Rather than specify a stress-strain law, we introduce a stored energy function (the compressible Neo-Hookean stored energy function [Ciarlet (1993)] suitably modified to account for viscoelasticity)

$$\begin{aligned} \psi(\mathbf{C}, \mathbf{Q}) = & \frac{1}{2} (\kappa \log[J])^2 + \underbrace{\frac{1}{2} \mu [J^{-2/3} \mathbf{C} : \mathbf{1} - 1]}_{\bar{\psi}} \\ & - \frac{1}{2} \mathbf{Q} : (J^{-2/3} \mathbf{C} - \mathbf{1}) + \psi_I(\mathbf{Q}). \end{aligned} \quad (14)$$

In the above function,  $\mathbf{Q}$  is a stress-like variable that models the viscoelastic response through the equations

$$\begin{aligned} \dot{\mathbf{Q}} + \frac{1}{\tau} \mathbf{Q} = & \gamma \frac{d}{dt} \left\{ \text{DEV} \left[ 2 \frac{\partial}{\partial (J^{-2/3} \mathbf{C})} \bar{\psi} \right] \right\} \\ \mathbf{Q}|_{t=0} = & 0, \end{aligned} \quad (15)$$

where, the parameter  $\gamma$  is a three-dimensional generalization of the ratio  $E/(E + E_{\infty})$  of the one-dimensional model, and the operator  $\text{DEV}(\cdot)$  picks the deviatoric component of a tensor. Details are provided in Simo and Hughes (1998). Additionally, the function  $\psi_I(\mathbf{Q})$  is written as,

$$\psi_I(\mathbf{Q}) = -\gamma \bar{\psi} + \frac{1}{2} \mathbf{Q} : (J^{-2/3} \mathbf{C} - \mathbf{1}), \quad (16)$$

and provides the proper conditions at thermodynamic equilibrium. The symbol  $\mathbf{1}$  denotes the identity tensor,  $\kappa$  and  $\mu$  are, respectively, the bulk and shear moduli and the symbol  $(\cdot) : (\cdot)$  indicates contraction of the corresponding tensors. The series of Eq. 14—16 summarizes the Standard Solid Viscoelastic model in the finite strain framework. The stress is now calculated as

$$\mathbf{S} = 4 \frac{\partial}{\partial \mathbf{C}} \psi(\mathbf{C}, \mathbf{Q}). \quad (17)$$

The stress  $\mathbf{S}$  introduced above is the Second Piola-Kirchhoff stress tensor and is related to the Cauchy stress by  $\mathbf{S} = \mathbf{F}^{-1} \mathbf{J} \boldsymbol{\sigma} \mathbf{F}^{-T}$ , and, to the nominal stress  $\mathbf{P}$  by  $\mathbf{P} = \mathbf{F} \mathbf{S}$ .

We have chosen not to enter into a detailed discussion of the viscoelastic model in the finite strain framework beyond the above outline. The interested reader is directed to the work of Simo and Hughes (1998) for an exhaustive treatment.

The Law of Mechanical Equilibrium for the static case is written as,

$$\text{DIV} \mathbf{P} + \mathbf{f} = 0, \quad (18)$$

where,  $\mathbf{f}$  denotes the body force. Since the stress is related to the displacement gradient, Eq. 18 can be restated with displacement as the fundamental variable. Boundary conditions are specified as,

$$\mathbf{u}|_{\partial\Omega_u} = \mathbf{g}, \quad \mathbf{P}\mathbf{F}^T \mathbf{n}|_{\partial\Omega_t} = \mathbf{t}, \quad (19)$$

where,  $\partial\Omega_u$  and  $\partial\Omega_t$  are, respectively, the parts of the boundary on which displacement and traction boundary conditions are specified.

#### 2.1.4 Expansion and the constitutive law

The expansion of thermally grown SiO<sub>2</sub> to 2.2× the volume of consumed Si is a fundamental material property of the oxide. Since, in the framework of continuum mechanics, the constitutive law is the proper vehicle for specification of material properties, it is natural to incorporate the expansion phenomena within this law. To arrive at such a law, we recall that in the description of oxidation implied by our treatment of the diffusion-reaction processes, Si material points are transformed to oxide and instantaneously expand. In the absence of hydrostatic pressure, the ratio of final to initial volume at the end of this expansion is 2.2. Conversely, when the pressure is non-zero, the volume ratio is different from 2.2. Another way of looking at this argument is that a volume expansion ratio of 2.2 gives zero pressure, while any departure from this value results in a pressure. Clearly, if the oxide has a volume ratio greater than 2.2, it is being stretched by a tensile pressure and vice-versa. Finally, we note that by definition, the volume ratio we are referring to is the jacobian  $J$ . In order to formalize the above arguments in mathematical language, a minor modification of the Neo-Hookean stored energy function in Eq. 14 is required. It is rewritten (using the same symbol  $\psi$  as,

$$\begin{aligned} \psi(\mathbf{C}, \mathbf{Q}) = & \frac{1}{2} (\kappa \log[J/2.2])^2 + \frac{1}{2} \mu [J^{-2/3} \mathbf{C} : \mathbf{1} - 1] \\ & - J^{-2/3} \mathbf{Q} : \mathbf{C} + \psi_I(\mathbf{Q}). \end{aligned} \quad (20)$$

The stress is still given as before, by Eq. 17.

#### 2.1.5 Stress dependence of diffusivity and reaction constant

The notions of stress-dependent diffusivity and reaction constants were introduced in Sec. 2.1.1. The specific forms adopted for the dependencies are discussed here. The diffusivity and reaction constant are written as,

$$\begin{aligned} D = & D_0 \exp\left(\frac{pV_d}{kT}\right) \\ k_s = & k_{s_0} \exp\left(\frac{pV_r}{kT}\right), \end{aligned} \quad (21)$$

where,  $D_0$  and  $k_{s_0}$  are the stress-free diffusivity and reaction constant respectively,  $V_d$  and  $V_r$  are the activation volumes corresponding to diffusion and reaction respectively,  $k$  is Boltzmann's constant and  $T$  is the temperature. The hydrostatic pressure is  $p$ , defined by  $p = (\sigma_{11} + \sigma_{22} + \sigma_{33})/3$ , (where  $\boldsymbol{\sigma}$  is the Cauchy stress) and is negative in compression. In contrast with earlier studies of the oxidation problem the reaction constant is enhanced or depressed by the pressure,  $p$ , rather than the normal stress  $\sigma_{nn}$  [see Rafferty (1989); Uchida, Fujinaga, Kotani, Kawazu, and Miyoshi (1996); Senez, Collard, Ferreira, and Baccus (1996); Navi and Dunham (1997) and references therein]. The justification for this difference follows: Earlier investigations treated the oxide expansion as a one-dimensional movement of the interface normal to itself. The stress opposing this expansion is the (compressive) normal stress  $\sigma_{nn}$ . The extra work to be performed in order to overcome the activation barrier is given by  $\sigma_{nn}V_r$ . In contrast, this study assumes isotropic expansion of the oxide. The stress component opposing such an expansion is the pressure in the oxide. Following a line of reasoning identical to that just advanced, the work to be performed in overcoming the activation barrier is  $pV_r$ . Thus, it is this factor that enhances or depresses the reaction constant. The choice of activation volumes will be dealt with in Sec. 3.

In summary, this subsection presents precise mathematical formulations of diffusion, reaction and mechanics. Importantly, these formulations are based on very well established and classical concepts in continuum mechanics.

## 2.2 Numerical methods

This section discusses the numerical methods which are applied to the mathematical formulations outlined in Sec. 2.1. This involves accurate numerical methods to treat the Hamilton-Jacobi equation for movement of the interface, interpolations capable of resolving discontinuous variations in concentration, and large, inhomogeneous expansions of a material. The finite element method is adopted as the basic discretization technique for all equations to be solved.

### 2.2.1 Numerical implementation of diffusion–reaction

For the diffusion-reaction problem, the primary variable is the concentration of the oxidant. A finite element discretization consisting of linear triangles is used. The concentration is solved for at the finite element nodes. Standard, linear interpolation functions are used. Such interpolations cannot reproduce discontinuous concentrations. Since the concentration of O<sub>2</sub> is discontinuous at the Si/SiO<sub>2</sub> interface, enhancements that resolve discontinuities on the SiO<sub>2</sub>-Si interface must be used in the interpolated field. The discontinuous interpolations have local support within elements and do not require element edges to be aligned with the Si/SiO<sub>2</sub> interface. Importantly, this ensures that the choice of mesh is not prejudiced by the interface. The interface, which is given by the set of points

with levelset contour  $\varphi = 0$ , moves as dictated by Eq. 7. A finite element formulation that allows the discontinuity associated with the interface to lie within elements eliminates the need for remeshing as the interface moves. In traditional formulations, the mesh must be changed after each time step as the interface moves. This leads often to meshes of very poor quality and incurs a significant computational cost. Details of the discontinuous interpolations and their derivation have been presented by Rao, Hughes, and Garikipati (1999). Here, we will only outline the idea in a very elementary fashion using a one dimensional example (see Fig. 2).

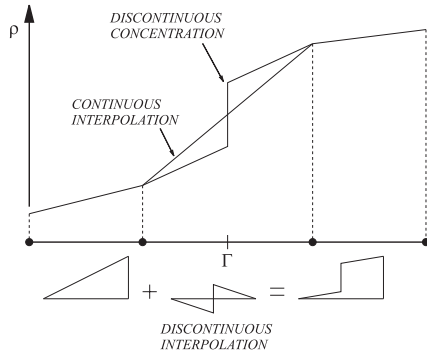


**Figure 2** : Example of one-dimensional diffusion with discontinuity in concentration across an interface,  $\Gamma$ . Note that the interface lies within the element and that concentration is continuous across elements.

Rao, Hughes, and Garikipati (1999) have shown that the complete concentration field can be expressed as

$$\rho = \sum_{a=1}^{n_{el}} (N_a + \tilde{N}l_a) c_a, \quad (22)$$

where,  $N_a$  and  $c_a$  are the nodal shape functions and concentrations respectively,  $n_{el}$  is the number of element nodes,  $\tilde{N}$  is a generalization to higher dimensions of the discontinuous interpolation in Fig. 2 and  $l_a$  denotes nodal values of a vector arising out of the flux and concentration discontinuities. The discontinuous interpolations were developed in the framework of the Enhanced Strain Finite Element Method. The interested reader is directed to the original work by Simo and Rifai (1990) for details and Rao, Hughes, and Garikipati (1999) for extensions to the diffusion problem.

### 2.2.2 Numerical implementation of the levelset equation

The evolution of the level set is governed by a time-dependent partial differential equation. In addition to a spatial discretization, it requires time discretization followed by integration. We first outline issues involved with the spatial discretization.

Eq. 7 is a pure advection equation (see Sec. 2). As is well known in the computational fluid dynamics community, standard numerical implementations of such equations show spurious spatial oscillations in the solution. A great body of work

has been written on “stabilizing techniques” for such systems of equations. Here, we adopt the Galerkin Least Squares (GLS) approach of Brooks and Hughes (1982); Hughes and Mallet (1986); Hughes, Franca, and Mallet (1987); Hughes, Franca, and Hulbert (1989); Johan, Hughes, and Shakib (1991); Brezzi and Russo (1994); Brezzi, Franca, Hughes, and Russo (1997) to stabilize the equation. To the original weak form of the equation,

$$\int_{\Omega} w \frac{\partial \varphi}{\partial t} dV + \int_{\Omega} w V_n \|\nabla \varphi\| dV = 0, \quad (23)$$

is added a term to yield a stabilized weak form:

$$\int_{\Omega} w \frac{\partial \varphi}{\partial t} dV + \int_{\Omega} w V_n \|\nabla \varphi\| dV + \underbrace{\tau \int_{\Omega} V_n \frac{\nabla \varphi}{\|\nabla \varphi\|} \nabla w V_n \|\nabla \varphi\| dV}_{\text{stabilizing term}} = 0. \quad (24)$$

Time integration is performed using the Forward Euler Method. For a time step  $\Delta t$  between time  $t_i$  and  $t_{i+1}$ , denoting quantities at time  $t_i$  by  $(\cdot)_i$ ; this algorithm furnishes an update according to the rule:

$$\varphi_{i+1} = \varphi_i + \Delta t (V_n \|\nabla \varphi_n\|)_i. \quad (25)$$

The Forward Euler algorithm has the advantage of resulting in an explicit method when combined with a diagonal mass matrix. Furthermore, in the above form it eliminates the necessity for an iterative scheme for the solution of the nonlinear advective equation. It is thus extremely attractive from the standpoint of computational efficiency. Observe that Eq.5 provides the velocity  $V_n$  only at points on the interface. A velocity projection scheme has been implemented for the purpose of determining  $V_n$  at points away from the interface.

### 2.2.3 Numerical implementation of the mechanics

In Sec. 2.1.3 it was shown that the finite strain formulation naturally leads to a nonlinear stress-strain law. It follows that any finite element implementation is also nonlinear in terms of the displacements. An iterative scheme, typically, the Newton-Raphson method or some variation thereof, needs to be adopted to solve this system of nonlinear equations. The equations are to be linearized at each iteration and an incremental update to the displacements is solved for. The assembled finite element equations that are solved then take the form:

$$\begin{aligned} \mathbf{f}_i^k + (\mathbf{K}_m^k + \mathbf{K}_g^k) \Delta \mathbf{d}_i^k &= 0 \\ \Rightarrow \Delta \mathbf{d}_i^k &= -(\mathbf{K}_m^k + \mathbf{K}_g^k)^{-1} \mathbf{f}_i^k \\ \mathbf{d}_{i+1}^{k+1} &= \mathbf{d}_i^k + \Delta \mathbf{d}_i^k. \end{aligned} \quad (26)$$

In Eq. 26,  $\mathbf{f}_i^k$  is the finite element residual at iteration  $k$  for time  $t_i$ ,  $\Delta \mathbf{d}_i^k$  is the incremental nodal solution vector at iteration  $k$  for

time  $t_i$  and  $\mathbf{K}_m$  and  $\mathbf{K}_g$  are, respectively, the material and geometric finite element stiffness matrices. The material tangent,  $\mathbf{K}_m$  is similar to the tangent stiffness matrix of the infinitesimal strain theory, while the geometric tangent,  $\mathbf{K}_g$  carries additional terms that account for large strains and large rotations, and, the contribution to the stiffness arising from their interaction with the stress. The interested reader is directed to the work of Simo and Hughes (1998) and references therein for details.

The viscoelastic evolution Eq. 15 needs to be integrated in time to solve for the stress-like variable  $\mathbf{Q}$ . Observing that the ordinary differential equation is of first order in time and linear, the integral can be written in convolution form as:

$$\mathbf{Q}(t) = \gamma \int_0^t \exp\left[\frac{s-t}{\tau}\right] \frac{d}{ds} \left( 2 \text{DEV} \left\{ \frac{\partial \psi}{\partial J^{-2/3} \mathbf{C}} \right\} \right) ds. \quad (27)$$

Eq. 27 involves integration over the entire history of the process to obtain the current value of  $\mathbf{Q}$ . A straightforward numerical implementation becomes prohibitively expensive over medium to large intervals of time. Instead, a two-point recurrence formula is adopted that only makes use of history values from the previous timestep to calculate  $\mathbf{Q}$  at the current time:

$$\mathbf{Q}_{n+1} = \mathbf{Q}_n \exp\left[\frac{-\Delta t}{\tau}\right] + \exp\left[\frac{-\Delta t}{2\tau}\right] \left( \text{DEV} \left\{ 2 \frac{\partial \psi}{\partial (J_{n+1}^{-2/3} \mathbf{C}_{n+1})} \right\} - \text{DEV} \left\{ 2 \frac{\partial \psi}{\partial (J_n^{-2/3} \mathbf{C}_n)} \right\} \right) \quad (28)$$

The formula in Eq. 28 is based on the midpoint rule. Accordingly, it is both second order accurate and unconditionally stable; both of which are extremely desirable properties for any time integration scheme. This formula was first proposed by Simo (1985).

The interface, in passing through an element, separates it into Si and SiO<sub>2</sub> regions. As discussed in Sec. 2.1.3, the material properties of Si and SiO<sub>2</sub> are very different. The differences lie in the viscoelastic behaviour of SiO<sub>2</sub> in contrast with elastic behaviour of Si and, additionally, the property of SiO<sub>2</sub> by which its pressure-free state is attained at a volume expansion ratio of 2.2. For Si, the pressure-free state is at a volume ratio of one. Different constitutive laws are specified for the Si and SiO<sub>2</sub> part of each element. Additionally, since the SiO<sub>2</sub> part must be allowed to expand much more than the Si, the Enhanced Strain Finite Element Method is used to enrich the strain field in the SiO<sub>2</sub>. This is done by way of interpolations which are local to the element and result in a larger volume strain (the jacobian,  $J$ ) in the SiO<sub>2</sub> region *within the same element*. The deformation gradient is enhanced as follows:

$$\mathbf{F}_e^h = \text{GRAD}[\phi_e^h] + \tilde{\mathbf{F}}_e^h. \quad (29)$$

In Eq. 29,  $\phi_e^h$  is the standard interpolation of the current position and  $\tilde{\mathbf{F}}_e^h$  is the enhancement to the deformation gradient.

The gradient with respect to the reference configuration is denoted  $\text{GRAD}[\cdot]$ . The superscript  $h$  denotes the fact that the quantities are finite dimensional approximations of the continuum ones and the subscript  $e$  indicates the local element. The enhancement to  $\mathbf{F}_e^h$ , i.e.,  $\tilde{\mathbf{F}}_e^h$  is chosen to represent a deformation gradient field incorporating an inhomogeneous volumetric strain over the element. With this enhancement, the method leads to the following modified weak form which arises from the Hu-Washizu variational principle:

$$\int_{\Omega} \text{GRAD} \boldsymbol{\eta}^h : \mathbf{P}^h dV - \int_{\Omega} \boldsymbol{\eta}^h \cdot \mathbf{f} - \int_{\partial \Omega_t} \boldsymbol{\eta}^h \cdot \mathbf{t} dS = 0, \quad (30)$$

$$\int_{\Omega_e} \tilde{\boldsymbol{\xi}}^h : \mathbf{P}^h dV = 0,$$

where,  $\boldsymbol{\eta}$  is the variation on the displacement field and  $\tilde{\boldsymbol{\xi}}$  is the corresponding variation on the enhanced deformation gradient,  $\tilde{\mathbf{F}}_e^h$ . The modified weak form thus consists of two equations, of which, Eq. 30 is to be satisfied for each element  $\Omega_e$ . The interested reader is directed to studies by Simo and coworkers Simo and Rifai (1990); Simo and Armero (1992); Simo, Armero, and Taylor (1993); Armero and Garikipati (1996) for details on the Enhanced Strain Finite Element Method.

The finite element implementation will be summarized to conclude this section: The equations governing diffusion-reaction, levelset evolution and quasistatic mechanical equilibrium are all solved using the same finite element mesh for spatial discretization of the equations. During the solution of the diffusion-reaction and mechanical equilibrium equations, the level set values are examined to determine whether a particular element has the interface passing through it. If so, Si and SiO<sub>2</sub> material properties are ascribed to the corresponding regions of the element. For the diffusion-reaction equation, discontinuous concentration interpolations are invoked. The internal residual is evaluated from the flux and the corresponding stiffness matrix is calculated. For the mechanical problem, viscoelastic and elastic constitutive laws are ascribed to the SiO<sub>2</sub> and Si regions. The volume strain is enriched as discussed above. The internal residual is calculated from the stress and its linearization provides the element material and geometric tangents. For the levelset equation, the appropriately evaluated normal velocity is used. The Galerkin Least Squares Method is employed to control spatial oscillations and the forward Euler time integration scheme is applied. The mass matrix and driving terms are evaluated. In each case the equations are assembled and a linear solve is performed. For the mechanical equilibrium equation an iterative scheme is employed until convergence is obtained. This convergence is typically measured by evaluating the magnitude of the global finite element residual which is driven to machine zero.

### 3 Incorporation of experimental data

This section deals with determination of the mechanical parameters of the Standard Solid Viscoelastic model followed by calibration of the growth parameters. This order to the extraction of parameters is important: the mechanical parameters are extracted from experimental stress data [Yu, Flinn, and Bravman (1996)]; once they are determined, the diffusion-reaction model is calibrated to growth data by varying the parameters  $D_0, k_{s0}, V_d$  and  $V_r$ . The incorporation of models for TEOS (Tetraethoxy Silane) shrinkage and density-relaxation of  $\text{SiO}_2$  during high temperature anneals is also discussed.

#### 3.1 Extraction of viscoelastic parameters

In this work, the extraction of mechanical parameters is based upon stress-strain data. This is in contrast with earlier investigations in which calibration parameters were adjusted to match growth data. As pointed out in Sec. 1, the earlier approaches admitted the possibility of having several parameter sets match the same data. Furthermore, there is no check to ensure that the mechanical parameters so determined will correspond well with stress-strain data.

The wafer curvature data of Yu, Flinn, and Bravman (1996) was used to extract mechanical parameters for  $\text{SiO}_2$ . In their experiments, approximately  $1\mu\text{m}$  of  $\text{SiO}_2$  was thermally grown on 100 mm, lightly p-doped  $\langle 100 \rangle$  Silicon substrates. Dry and wet ambients were used. Subsequently, the wafers were cooled down and isothermally annealed at temperatures ranging between  $800^\circ\text{C}$  and  $1000^\circ\text{C}$ . The stress due to mismatch in coefficients of thermal expansion induced curvature in the wafer, which was measured. Stoney's equation was applied to calculate the  $\text{SiO}_2$  film stress. The results demonstrated stress relaxation with time — indicative of viscoelastic behavior.

The Standard Solid Viscoelastic model outlined in Sec. 2.1.3 was used to calculate the stress arising out of the mismatched thermal strain. Since the strains involved in this case were small (for  $\alpha_{\text{Si}} = 3 \times 10^{-6}$  and  $\alpha_{\text{SiO}_2} = 0.55 \times 10^{-6}$  and a temperature change of  $\approx -350^\circ\text{C}$  the mismatched thermal strain is  $8.75 \times 10^{-4}$ ), the infinitesimal strain theory could be used, thereby simplifying the calculations. The biaxial stress developed in the film is

$$\sigma = \left\{ \kappa + \frac{4\mu}{3} \left( \gamma_\infty + \gamma \exp \left[ -\frac{t}{\tau} \right] \right) \right\} (\alpha_{\text{Si}} - \alpha_{\text{SiO}_2}) \Delta T, \quad (31)$$

where,  $\gamma_\infty = 1 - \gamma$ . This equation is used to determine  $\kappa, \mu, \gamma$  and  $\tau$  by way of a least squares error fit with the stress relaxation curves of Yu et al. (see Fig. 3 and 4).

Since the data in Fig. 3 and 4 represents stress relaxation of  $\text{SiO}_2$  at various temperatures, the variation with temperature of the extracted parameters is also obtained.

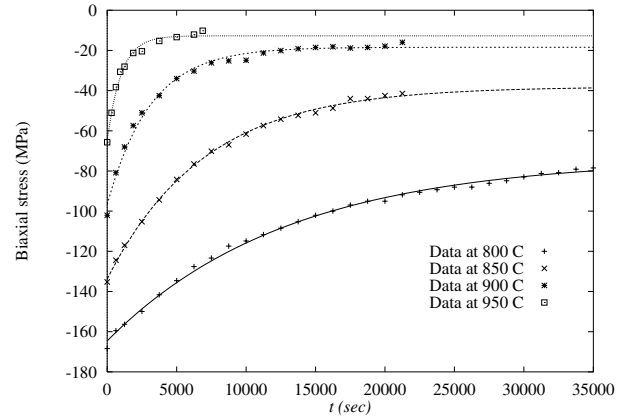


**Figure 3** : Fits to the isothermal relaxation data of Yu et al. using the standard solid viscoelastic model. The oxide was thermally grown dry at  $1150^\circ\text{C}$  and subsequently annealed at the indicated temperatures.

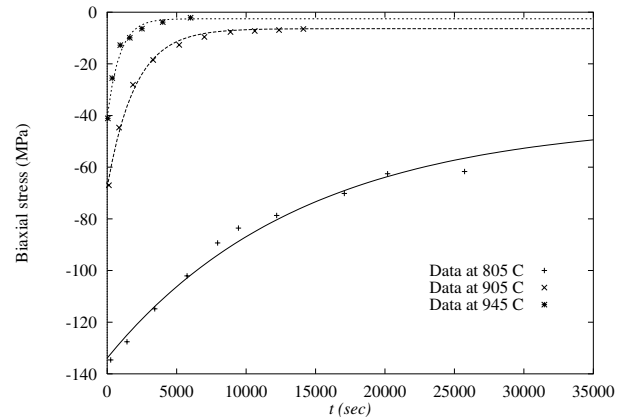


**Figure 4** : Fits to the isothermal relaxation data of Yu et al. using the standard solid viscoelastic model. The oxide was thermally grown wet at  $1150^\circ\text{C}$  and subsequently annealed at the indicated temperatures.

#### 3.2 Calibration to growth data

Since the mechanical model employed for this investigation differs from that in earlier investigations, the stress is also expected to be different. Since stress affects the growth of  $\text{SiO}_2$ , the corresponding parameters (the activation volumes,  $V_d$  and  $V_r$ ) must be recalibrated. In addition, for the present study the stress-free state of  $\text{SiO}_2$  does not correspond to planar growth. In earlier models, the diffusivity and reaction constant for planar growth; i.e., growth on a flat wafer have been taken as the corresponding stress-free values. These values have been calculated from Deal-Grove parameters, themselves extracted from experimental observations. For this study, the true stress-free diffusivity and reaction-constant are also treated as calibration parameters. The set  $\{D_0, k_{s0}, V_d, V_r\}$  was fixed by fit-

ting the model to growth data of Kao (1986). The resulting values appear in Tab. 1.

**Table 1** : Stress-free values of diffusion-reaction parameters

Property	Value
$D_0$	$6.999 \exp[-6 \times 10^{-12} T] \text{ (cm}^2 - \text{sec}^{-1}), T \text{ in K}$
$k_{s0}$	$5.532 \exp[-3 \times 10^{-12} T] \text{ (cm} - \text{sec}^{-1}), T \text{ in K}$
$V_d$	$30A^3$
$V_r$	$3A^3$

### 3.3 Shrinkage of TEOS

In the STI process, isolation of active Si areas is provided by dielectric filler materials. TEOS is a favored candidate for this purpose. Following the deposition of trench fill material (assumed to be TEOS), it is annealed in order to ensure densification. During this process chemical reactions take place resulting in the formation of  $\text{SiO}_2$  and release of byproducts such as  $\text{H}_2\text{O}$ . As a consequence, the filler material shrinks. On account of its being attached to the liner oxide, stress arises in the active areas adjacent to the trench walls and on the trench floor. Stademüeller (1992) has performed experimental studies of the densification process of various deposited films and catalogued the observed volume shrinkage and film stress. For the purpose of incorporation in a constitutive model, the stress-free shrinkage of TEOS (or, any other filler material) is necessary. Such information can then be incorporated into the model as in Sec. 2.1.4 leading to a further modification of Eq. 20:

$$\begin{aligned} \psi(\mathbf{C}) = & \frac{1}{2} \left( \kappa \log \left[ \frac{J}{2.2\beta} \right] \right)^2 + \frac{1}{2} \mu \left[ J^{-2/3} \mathbf{C} : \mathbf{1} - 1 \right] \\ & - \frac{1}{2} \mathcal{Q} : \left( J^{-2/3} \mathbf{C} - \mathbf{1} \right) + \psi_I(\mathcal{Q}), \end{aligned} \quad (32)$$

where,  $\beta$  is the volume shrinkage ratio ( $0 < \beta < 1$ ).

### 3.4 Density relaxation of $\text{SiO}_2$ during annealing

In addition to the volume expansion of thermal  $\text{SiO}_2$  and shrinkage of TEOS, there remains one phenomenon of volume change to be modelled: Experiments have shown that the structure of  $\text{SiO}_2$  undergoes a relaxation in density when annealed at high temperatures. The density has been observed to decrease — alternatively, the volume increases — by as much as 3–4% between  $600^\circ\text{C}$  and  $1050^\circ\text{C}$ . Given the low coefficient of thermal expansion of  $\text{SiO}_2$ ; i.e.,  $0.55 \times 10^{-6} \text{ }^\circ\text{C}^{-1}$ , this volume-increase cannot be attributed to thermal expansion.

Irene, Tierney, and Angilello (1982) treated this relaxation within the framework of a Maxwell viscoelastic model. The increase in volumetric strain was viewed as being driven by the relaxation of the compressive growth stress. This approach has also been adopted by Navi and Dunham (1997). In contrast, the viscoelastic model assumed in this work treats the hydrostatic pressure-component of the stress as being purely elastic. Instead, a phenomenological approach has been adopted. Turning to the work of Taniguchi, Tanaka, and Hamaguchi (1990), an evolution law is used for the volume strain during annealing. The law is summarized in the following equations:

$$\vartheta(t) = \frac{(n_0 - 1)^\alpha}{(n_\infty - 1 + (n_0 - n_\infty) \exp[-(t/\tau)^a])^\alpha} \quad (33)$$

$$\bar{\tau}(T) = \bar{\tau}_0 \exp(E_A/kT) \quad (34)$$

$$\bar{\tau}_0 = 1.26 \times 10^{-21} \text{ s} \quad (35)$$

$$E_A = 6 \text{ eV}. \quad (36)$$

Here,  $\vartheta(t)$  is the volumetric expansion ratio,  $n$  is the refractive index and subscripts  $(\cdot)_0$  and  $(\cdot)_\infty$  refer to initial and final values of the corresponding quantities. Suitable values of the exponents are  $\alpha = 0.17$  and  $a = 1.63$ . This contribution to the volumetric expansion ratio has been treated as an internal variable [see Lubliner (1990) for a discussion of the thermodynamic basis of internal variables]. In such a framework, the irreversibility of this volume expansion is easily ensured. Incorporating  $\vartheta(t)$  in the stored energy function, its final form is written as

$$\begin{aligned} \psi(\mathbf{C}) = & \frac{1}{2} \left( \kappa \log \left[ \frac{J}{2.2\beta\vartheta} \right] \right)^2 + \frac{1}{2} \mu \left[ J^{-2/3} \mathbf{C} : \mathbf{1} - 1 \right] \\ & - \frac{1}{2} \mathcal{Q} : \left( J^{-2/3} \mathbf{C} - \mathbf{1} \right) + \psi_I(\mathcal{Q}), \end{aligned} \quad (37)$$

## 4 Model validation

The aim of this section is to demonstrate the validity of the models introduced in Sec. 2 and 3. At issue is the correct representation of stress in qualitative and quantitative terms. By “qualitative correctness” is meant the development of compressive and tensile components of the stress tensor in order that the trends of experimentally observed phenomena be reproduced. “Quantitative correctness” applies to actual stress values. In what follows, the qualitative aspects will be demonstrated via development of wafer curvature during thermal oxidation and the attainment of the proper sign of stress components in STI process sequences. Microraman stress measurements provide validation of the models in terms of the actual stress values calculated. Plane strain conditions have been assumed for all examples. This implies that material points on the structures are assumed not to experience any displacement in the direction normal to the plane of the page.

#### 4.1 Wafer curvature

A model problem is considered (see the schematic in Fig. 5). A wafer of dimensions  $5\mu\text{m}$  (width) and  $1\mu\text{m}$  (thickness) is oxidized on its top surface. The oxidation is carried out dry at  $1000^\circ\text{C}$ . A Dirichlet boundary condition for diffusion is specified on the top surface in terms of the solubility of  $\text{O}_2$  in a dry ambient. Additionally, zero flux (Neumann) boundary conditions are specified on the remaining three surfaces. A thin layer of  $\text{SiO}_2$  is assumed to exist at the beginning of the problem (Fig. 6). Using symmetry, one half of the problem is solved for. This implies symmetry boundary conditions on the left vertical surface to restrain horizontal motion. Additionally, the right lower corner is prevented from vertical motion. This eliminates rigid body motions of the wafer.

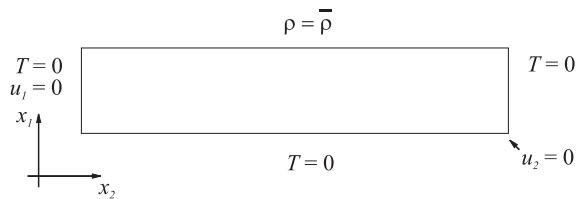
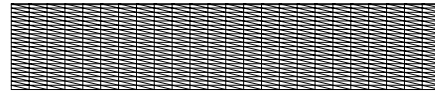


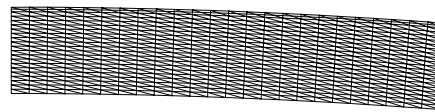
**Figure 5** : Schematic representation of the boundary value problem for wafer bending

This example aims at demonstrating the mechanically correct representation of oxide expansion. Wafers undergoing thermal oxidation on one surface bend away from that surface on account of the growth stress of the newly formed oxide. This oxide is in compression, and, on going through the derivation of Stoney's equation for a thin film on a substrate, it is readily apparent that the wafer does indeed curve away from the film. As discussed earlier, models that represent oxide expansion as a one-dimensional phenomenon (i.e., expansion only in the direction normal to the interface) cannot represent wafer curvature. It is the multidimensional expansion of the oxide that is responsible for wafer curvature during thermal oxidation. The present model demonstrates this very well. Fig. 6 shows the initial position of the interface. There is no bending in this figure since the solution has not been started. Fig. 8 shows a stage well into the oxidation. The interface has advanced into the substrate. The newly formed oxide has expanded and this expansion results in the expected wafer curvature. Fig. 9 shows the stress  $\sigma_{11}$ , where the  $x_1$  direction is along the length of the wafer. Negative stresses are compressive and vice versa. The newly-formed  $\text{SiO}_2$  is restrained from attaining its stress-free volume by the substrate and is therefore in compression. This compressive stress results in a tensile stress in the substrate just below the interface. On moving further away from the interface, the effect of the wafer's curvature results in the substrate stress changing from tension to compression. This is exactly what would be expected from this problem.



Time = 0.00E+00

**Figure 6** : Unoxidized wafer with a very thin initial layer ( $10\text{\AA}$ ) of  $\text{SiO}_2$



Time = 3.00E+03

**Figure 7** : Deformed mesh after 50 minutes of oxidation at  $1000^\circ\text{C}$  in a dry ambient. Observe movement of the interface into the substrate and the beginning of bending.

#### 4.2 Computation of stress in an STI process

A numerical example is presented to demonstrate calculations for the entire STI process. Each stage of the process is solved for, accounting for thermal oxidation, deposition or removal of material and the accompanying mechanics. Variation in thermal stress, material moduli and diffusion-reaction parameters with temperature and temperature ramps, as discussed in previous sections, are also included.

A test structure consisting of an array of  $4\mu\text{m}$  lines separated by  $4\mu\text{m}$  trenches is considered (Fig. 10). Symmetry is invoked to allow the solution to be carried out on the region within the dotted lines. Accordingly, the extreme left and right vertical faces of the structure are constrained from having horizontal displacements and the bottom surface is constrained from vertical displacements. The boundary conditions for the diffusion-reaction problem and the initial condition for the levelset evolution equation will change with the process step.

##### 4.2.1 Thermal growth of barrier oxide

This first stage of the STI process sequence is carried out on a substrate  $4\mu\text{m}$  in width and  $0.7\mu\text{m}$  in thickness. Oxidation in a dry ambient at  $920^\circ\text{C}$  is assumed. A thin layer of barrier

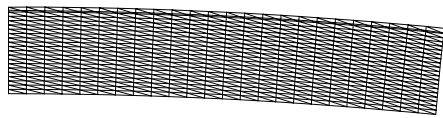


**Figure 8** : Deformed mesh after 100 minutes of oxidation at 1000° C in a dry ambient. Observe small amount of further movement of the interface and more pronounced bending. The outermost layer of elements is undergoing a small amount of expansion which is not noticeable in this figure.

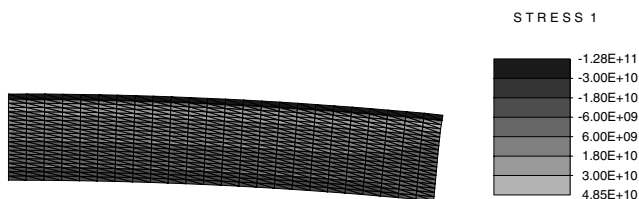


**Figure 9** : Contour plot of  $\sigma_{11}$  after 100 minutes of oxidation.

oxide is grown on the upper surface. Fig. 11 and 12 show the materials and stress,  $\sigma_{11}$  at the end of this step.

#### 4.2.2 Nitride deposition

A layer of nitride,  $0.15\mu\text{m}$  thick, is deposited over the barrier oxide at  $740^\circ\text{C}$ . This step is modelled by accounting for the shrinkage in volume experienced by deposited nitride. It is assumed that this volume shrinks by 5% in a stress-free state [Stademüeller (1992) reports a value of 3%, but this is in a stressed state]. This shrinkage results in a new state of stress in the entire structure which is solved for starting from the state of stress at the end of the barrier oxidation step, lowering the temperature and specifying the shrinkage of nitride. The oxide is assumed to be purely elastic below  $750^\circ\text{C}$ . It is further assumed that the entire thickness of the nitride is deposited instantaneously. A gradual process could also be modelled wherein incremental nitride layers are deposited and the calculations for stress equilibrium are performed after the addition of each new layer. Fig. 13 and 14 show the materials and stress at the end of this step. Note that the diffusion-reaction and levelset evolution problems do not play a role in this step.

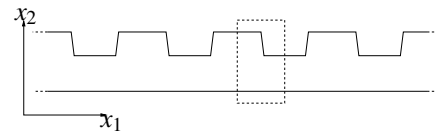


**Figure 10** : Schematic representation of an array of lines and a section chosen to compute the solution on the basis of symmetry.



**Figure 11** : Materials after growth of barrier oxide: Substrate (grey) and barrier oxide (black)

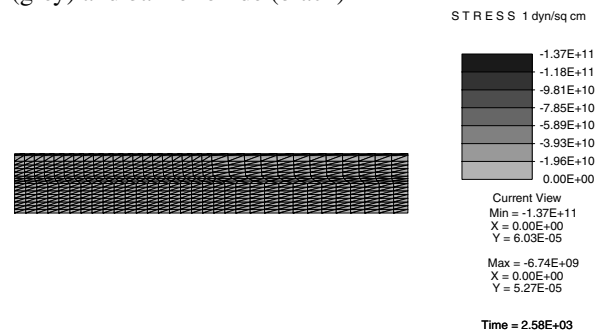


**Figure 12** :  $\sigma_{11}$  at the end of barrier oxide growth

#### 4.2.3 Trench etch

This step is modelled by removing material (nitride, oxide and substrate) to leave a trench of width  $4\mu\text{m}$  with a sidewall slope of about  $87^\circ$ . As in the nitride deposition step, only a new state of stress needs to be calculated. Again, this is numerically modelled by assuming that the trench is instantaneously etched rather than accounting for the incremental process. The solution for an incremental etch would be carried out as discussed in Sec. 4.2.2. The etch is assumed to occur at  $55^\circ\text{C}$ .

#### 4.2.4 Liner oxidation

Following the trench etch, liner oxidation is carried out in a dry ambient at  $1000^\circ\text{C}$ . In this step, the full thermal oxidation problem is solved. We point out that this stage involves the specification of a new set of boundary conditions for the diffusion-reaction problem. The trench wall and floor have oxidant concentration specified by accounting for solubility of  $\text{O}_2$  in a dry ambient, and, the remaining free surfaces have zero flux boundary conditions. The initial condition for the levelset evolution equation also must be specified afresh to represent a thin layer of oxide along the trench wall and floor. Fig. 17 and 18 show the materials and stress at the end of this stage.



**Figure 13** : Materials after nitride deposition: Substrate (light grey), barrier oxide (black) and nitride mask (dark grey)

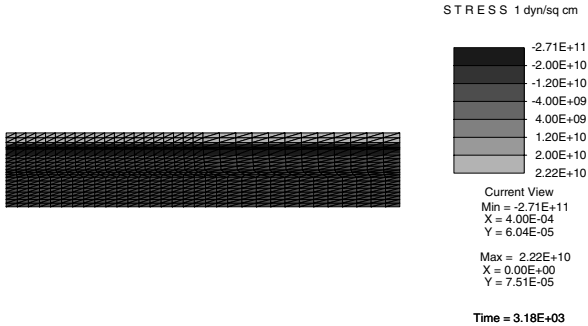


**Figure 14** :  $\sigma_{11}$  at the end of nitride deposition. 5% densification assumed for nitride, which is modelled as an elastic solid in this case. The stress represented is that after deposition of nitride and attainment of a new mechanical equilibrium state for the entire structure.

#### 4.2.5 TEOS deposition and shrinkage

Subsequent to liner oxidation, trench-fill TEOS is deposited at 650°C. Given the profile of the structure at the end of liner oxidation, the profile of trench fill TEOS is solved by a two-dimensional topography algorithm (the code SPEEDIE [SPE (1995)] was used) to generate a highly conforming profile. For this calculation, it was assumed that the shrinkage associated with the reactions (by which TEOS gives rise to SiO<sub>2</sub> and H<sub>2</sub>O) does not produce a stress. However, the annealing-related volume expansion (see Sec. 3.4) of SiO<sub>2</sub> does cause stress. This property is attributed to both thermally grown SiO<sub>2</sub> and SiO<sub>2</sub> from deposited TEOS. As discussed above for nitride deposition (Sec. 4.2.2), stress equilibrium is solved for on the full structure. Fig. 19 and 20 show the materials and stress at the end of this stage.

#### 4.2.6 TEOS polish

This step is modelled by removal of the TEOS down until the nitride level. The new state of stress is calculated at 70°C by assuming - as with the earlier stages involving material removal - that all the material is removed instantaneously. Fig. 21 and 22 show the materials and stress at the end of the TEOS polish step.

#### 4.2.7 Nitride strip

This stage is solved for at 140°C. It is assumed that the adjacent trench-fill is also planarized. Fig. 23 and 24 show the materials and stress.



**Figure 15** : Materials after trench etch: Substrate (light grey), barrier oxide (black) and nitride mask (dark grey)

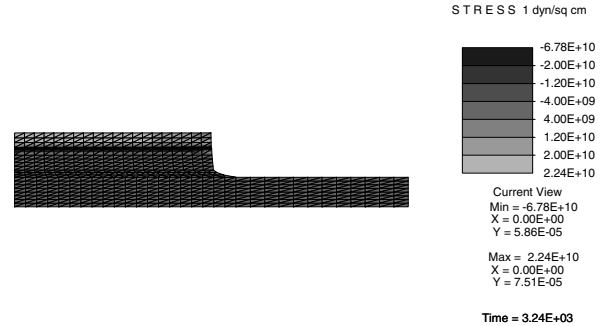


**Figure 16** :  $\sigma_{11}$  at the end of trench etch. The stress represented is that after trench etch and attainment of a new mechanical equilibrium state for the entire structure.

#### 4.2.8 Sacrificial oxide growth

A layer of sacrificial oxide is thermally grown over the active region. This results in the thickening of the existing oxide which was originally grown in the barrier oxidation step. Sacrificial oxide growth is considered at 910°C in a dry ambient. The boundary conditions for the diffusion-reaction problem are respecified in the form of concentration over the active area and zero flux on the remaining free surfaces. The initial condition for the levelset evolution equation is specified by accounting for the position of the barrier oxide/substrate interface. Fig. 25 and 26 show the materials and stress at the end of this stage.

#### 4.2.9 Sacrificial oxide strip

This stage is modelled at 306°C. Here it is assumed that the adjacent trench-fill material is not planarized in the process. The sacrificial oxide is removed and stress equilibrium is solved for.

#### 4.2.10 Thermal growth of gate oxide

The final stage in the STI process sequence considered here is the growth, at 900°C, of a thin layer of gate oxide over the active area. The oxidant concentration is specified on the newly exposed upper surface of the active area. The initial condition for the levelset evolution equation is also specified by accounting for the thickness of the sacrificial oxide left at the end of the stripping stage (Section 4.2.9).

### 4.3 Validation of STI stress

This section presents a comparison between micro-Raman Spectroscopy measurements on the test structure described in

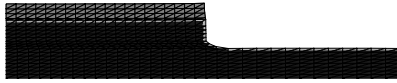


Figure 17 : Materials after liner oxidation: Substrate (black), barrier/liner oxide (lightest grey) and nitride mask (light grey)

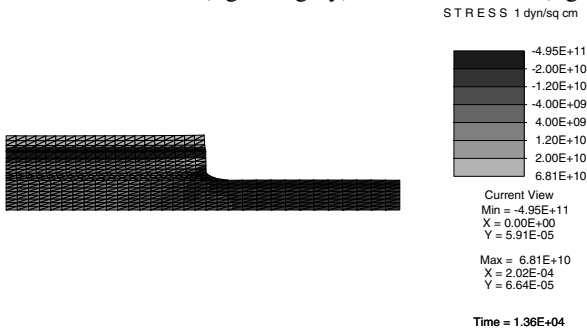


Figure 18 :  $\sigma_{11}$  at the end of liner oxide growth

Sec. 4.2 and a numerical solution of the full STI process sequence upon a section of the test structure. The section chosen out of the test structure corresponds to that depicted in Fig. 10. The principles and procedure of using Microraman Spectroscopy to measure the stress in a Silicon structure have been discussed extensively in the work of de Wolf, Norström, and Maes (1993); de Wolf, Maes, and Jones (1996); Jain, Maes, Pinardi, and de Wolf (1996); de Wolf, Pozzati, Pinardi, Howard, Ignat, Jain, and Maes (1996); de Wolf (1996). A brief description follows:

The frequency of the Si Raman peak depends on stress. In order to determine this frequency, the peak is fitted with a Lorentzian function. The plasma lines of the laser are used as reference. They are fitted using a Gaussian function to determine their frequency. In the present case, the structure was scanned in a direction perpendicular to the lines. The measurements were made in backscattering from the (100) surface. A laser with wavelength 457.9 nm and output power 40 mW was used. With certain assumptions, the Raman shift can be related to the normal stress perpendicular to the line. Instead, the reverse was done; the Raman shift was evaluated on the basis of the numerical solution for the local strain and compared with the actual measurement. On the basis of the work of de Wolf (see above references), the relation between band shift and stress is  $\sigma_{11} = -0.5 \times 10^9 \Delta\omega$ , where,  $\sigma_{11}$  is the normal Cauchy stress in Pa in the  $x_1$  direction and  $\Delta\omega$  is the shift in bandwidth in  $\text{cm}^{-1}$ .

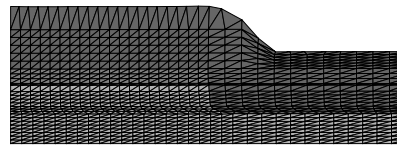


Figure 19 : Materials after TEOS deposition: Substrate (lightest grey), barrier oxide (black), nitride mask (lighter grey) and filler (grey) (liner oxide is not shown)

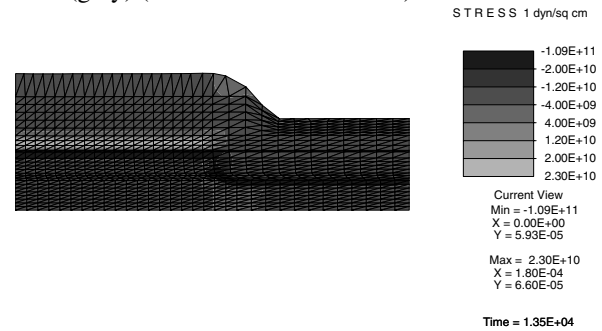
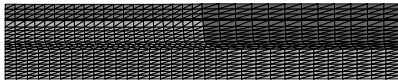
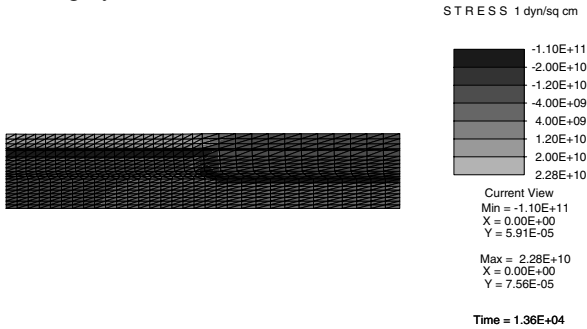


Figure 20 :  $\sigma_{11}$  at the end of filler deposition. 5% densification (literature values). The stress represented is that after deposition of TEOS and attainment of a new mechanical equilibrium state for the entire structure.

Results are shown in Fig. 31 and 32 for the Raman shifts after liner oxidation and the final gate oxidation respectively. The Raman shift is measured in Silicon just below the oxide. On the basis of the above discussion, it is clear that an accurate calculation of the Raman shift entails accurate modelling of stress. Thus, the model provides a reasonably correct stress field for the stage following liner oxidation. However, from a comparison of the band shift, it is clear that the stress predicted at the end of gate oxidation does not match as well with experiment. In particular, it is apparent from the plots that the stress calculated by the model in the line is higher than experimental values. This effect is particularly pronounced as the trench wall (where thermally grown and deposited  $\text{SiO}_2$  are in contact) is approached. At the present stage of this work, the viscoelastic properties obtained for thermally grown  $\text{SiO}_2$  (Sec. 3.1) have also been used for  $\text{SiO}_2$  deposited as TEOS. However, the mechanical properties of deposited films are known to vary significantly from those of thermally grown films. This would indicate that measurements of the viscoelastic properties of deposited  $\text{SiO}_2$  are necessary. Such an experimental program is being planned. It is expected that with such data, the stress predicted by the present models will correspond more closely with experiments. These experimental investigations will also be extended to examine the validity of the model of Taniguchi, Tanaka, and Hamaguchi (1990) for volume expansion of  $\text{SiO}_2$  when annealed. A further source of modelling-error is that perfect boundary conditions were assumed for the vertical boundaries in the mechanical problem (see Sec. 4.2). However, the wafer is almost certainly warp-



**Figure 21** : Materials after TEOS polish: Substrate (lightest grey), barrier oxide (black), nitride mask (lighter grey) and filler (grey) (liner oxide is not shown)



**Figure 22** :  $\sigma_{11}$  at the end of TEOS polish. The stress represented is that after removal of TEOS and attainment of a new mechanical equilibrium state for the entire structure.

ing as a consequence of oxidation of Silicon and annealing of  $\text{SiO}_2$ . This would involve some rotation of the boundaries. Investigations are underway on how best to represent the boundary conditions for the mechanical problem.

In contrast with the situation described above, the numerical solution at the end of liner oxidation shows better correspondence with the experimental result for bandwidth-shift. In this case, since the trench has yet to be filled, the problem of dissimilar materials does not arise.

The trends seen in the numerical solutions in Fig. 31 and 32 match well with experiment. They indicate compressive stress in the line, changing sharply to tension under the trench.

## 5 Conclusions

Models have been presented for the processes of diffusion-reaction, interface movement and mechanics involved in shallow trench isolation. It is evident that the complexity of the problem merits a rigorous treatment from the mathematical and numerical standpoint. The formalism of continuum mechanics and accompanying balance laws has been brought to bear upon the problem. Finite strain kinematics has been argued for and applied in modelling the large expansion of  $\text{SiO}_2$ . Various experimentally observed phenomena that contribute to the mechanics of the problem have been accounted for in a rigorous manner. The computational methods employed have been demonstrated to have the capability of calculating the stress at each step of the process. Qualitative and quantitative validation of the models has been presented.

The problem would benefit from the extension of the mathematical, mechanical and numerical models to three dimensions to account for effect such as those at corners. In addition, fur-



**Figure 23** : Materials after nitride strip: Substrate (lighter grey), barrier oxide (black) and filler (grey) (liner oxide is not shown)

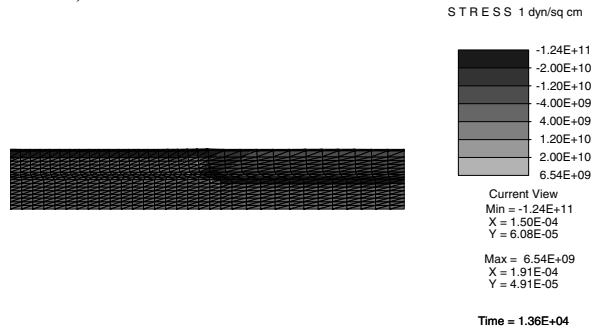


**Figure 24** :  $\sigma_{11}$  at the end of nitride strip. The stress represented is that after stripping of nitride and attainment of a new mechanical equilibrium state for the entire structure.

ther experimentation is needed to obtain data on aspects such as expansion of  $\text{SiO}_2$  under annealing. The appropriate mechanical boundary conditions appear to need further investigation.

**Acknowledgement:** This work was jointly supported by AMD Inc. and the Center for Integrated Systems, Stanford University. This support is greatly appreciated.

## References

- Armero, F.; Garikipati, K.** (1996): An analysis of strong discontinuities in multiplicative finite strain plasticity and their relation with the numerical simulation of strain localization in solids. *Int. J. Solids and Structures*, vol. 33, no. 20-22, pp. 2863–2855.
- Brezzi, F.; Franca, L. P.; Hughes, T. J. R.; Russo, A.** (1997):  $\mathbf{b} = \int \mathbf{g}$ . *Comp. Methods in Applied Mech. Engrg.*, vol. 145, pp. 329–339.
- Brezzi, F.; Russo, A.** (1994): Choosing bubbles for advection-diffusion problems. *Math. Models Math. App. Sci.*, vol. 4, no. 4, pp. 571–587.
- Brooks, A.; Hughes, T.** (1982): Streamline upwind/Petrov-Galerkin formulations for convection dominated flows with particular emphasis on the incompressible Navier-Stokes equations. *Comp. Methods in Applied Mech. Engrg.*, vol. 32, pp. 199–259.
- Cea, S.; Law, M.** (1996): Three dimensional nonlinear viscoelastic oxidation modeling. In *International Conference on Simulation of Semiconductor Processes and Devices, SISPAD, IEEE, Tokyo, Japan*, pp. 97–98.



**Figure 25 :** Materials after sacrificial oxide growth: Substrate (black), barrier/liner oxide (lighter grey) and filler (grey)

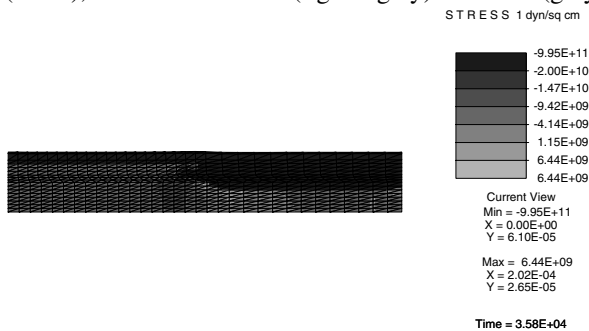


**Figure 26 :**  $\sigma_{11}$  at the end of sacrificial oxide growth



**Figure 27 :** Materials after sacrificial oxide strip: Substrate (black), liner oxide (lighter grey) and filler (grey)

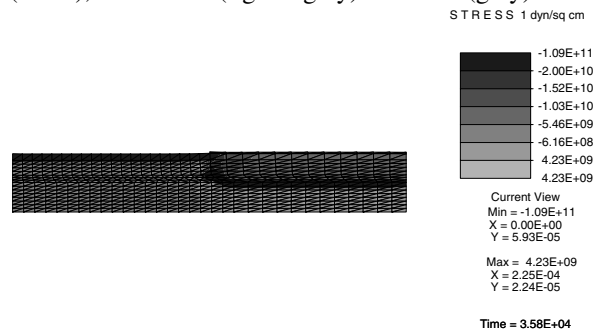


**Figure 28 :**  $\sigma_{11}$  at the end of sacrificial oxide strip

**Chadwick, P.** (1976): *Continuum Mechanics: Concise Theory and Problems*. John Wiley & Sons.

**Chang, C.; et al.** (1997): A highly manufacturable corner rounding solution for 0.18 micron shallow trench isolation. *IEDM Tech. Digest*, pp. 661–664.

**Chin, D.** (1983): Two-dimensional oxidation. *Ph.D. Thesis, Stanford University*.

**Ciarlet, P.** (1993): *Mathematical Elasticity*. North Holland.

**de Wolf, I.** (1996): Micro-Raman spectroscopy to study local mechanical stress in silicon integrated circuits. *Semicond. Sci. Technol.*, vol. 11, pp. 139–154.

**de Wolf, I.; Maes, H. E.; Jones, S. K.** (1996): Stress measurements in silicon devices through Raman spectroscopy: Bridging the gap between theory and experiment. *J. Applied Physics*, vol. 79, no. 9, pp. 7148–7156.

**de Wolf, I.; Norström, H.; Maes, H. E.** (1993): Process-induced stress in isolation structures studied by micro-Raman spectroscopy. *J. Applied Physics*, vol. 74, no. 7, pp. 4490–4500.

**de Wolf, I.; Pozzati, G.; Pinardi, K.; Howard, D. J.; Ignat, M.; Jain, S. C.; Maes, H. E.** (1996): Experimental validation of mechanical stress models by micro-Raman spectroscopy. *Microelectron. Reliab.*, vol. 36, no. 11/12, pp. 1751–1754.

**Deal, B.; Grove, A. S.** (1965): General relationship for the thermal oxidation of silicon. *J. Appl. Physics*, vol. 36, no. 12, pp. 3370–3378.

**Dutton, R. W.** (1983): Modeling of the silicon integrated-circuit design and manufacturing processes. *SIAM J. Sci. Stat. Comp.*, vol. 4, no. 3, pp. 357–390.

**EerNisse, E.** (1979): Stress in thermal SiO<sub>2</sub> during growth. *Appl. Phys. Lett.*, vol. 35, no. 1, pp. 8.

**Eyring, H.** (1936): Viscosity, plasticity and diffusion as examples of absolute reaction rates. *J. Chemical Physics*, vol. 4.

**Fahey, P. M.; Mader, S. R.; Stiffler, S. R.; Mohler, R. L.; Mis, J. D.; Slinkman, J. A.** (1992): Stress-induced dislocations in silicon integrated circuits. *IBM J. Res. Develop.*, vol. 36, no. 2, pp. 158–182.

**Green, A.; Zerna, W.** (1954): *Theoretical Elasticity*. Clarendon Press, Oxford.

**Gurtin, M.** (1981): *An Introduction to Continuum Mechanics*. Academic Press.

**Hsueh, C.; Evans, A.** (1983): Oxidation induced stress and some effects on the behavior of oxide films. *J. Appl. Physics*, vol. 54, no. 11.



**Figure 29** : Materials after growth of gate oxide: Substrate (black), gate/liner oxide (lighter grey) and filler (grey)

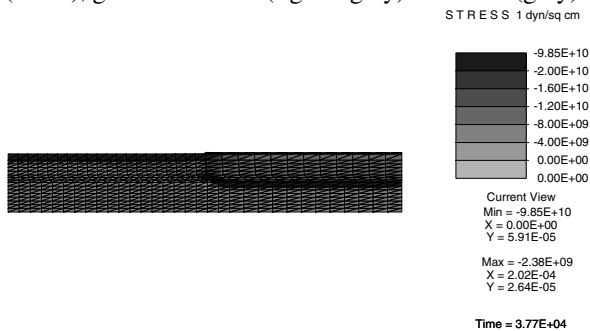


**Figure 30** :  $\sigma_{11}$  at the end of gate oxide growth

**Hu, S.** (1991): Stress-related problems in silicon technology. *J. Applied Physics*, vol. 70, no. 6, pp. R53–R80.

**Hughes, T.; Franca, L.; Hulbert, G.** (1989): A new finite element formulation for computational fluid dynamics: VIII. The Galerkin/least-squares methods for advective–diffusive equations. *Comp. Methods in Applied Mech. Engrg.*, vol. 73, pp. 173–189.

**Hughes, T.; Franca, L.; Mallet, M.** (1987): A new finite element formulation for computational fluid dynamics: VII. Convergence analysis of the generalized SUPG formulation for linear time-dependent multidimensional advective–diffusive systems. *Comp. Methods in Applied Mech. Engrg.*, vol. 63, no. 1, pp. 97–112.

**Hughes, T. J. R.; Mallet, M.** (1986): A new finite element formulation for computational fluid dynamics: III. The generalized streamline operator for multidimensional advective–diffusive flows. *Comp. Methods in Applied Mech. Engrg.*, vol. 58, no. 3, pp. 305–328.

**Irene, E.; Tierney, E.; Angiello, J.** (1982): A viscous flow model to explain the appearance of high density thermal SiO<sub>2</sub> at low oxidation temperatures. *J. Electrochem. Soc.*, vol. 129, pp. 2594–2597.

**Jain, S. C.; Maes, H. E.; Pinardi, K.; de Wolf, I.** (1996): Stress and strains in lattice-mismatched stripes, quantum

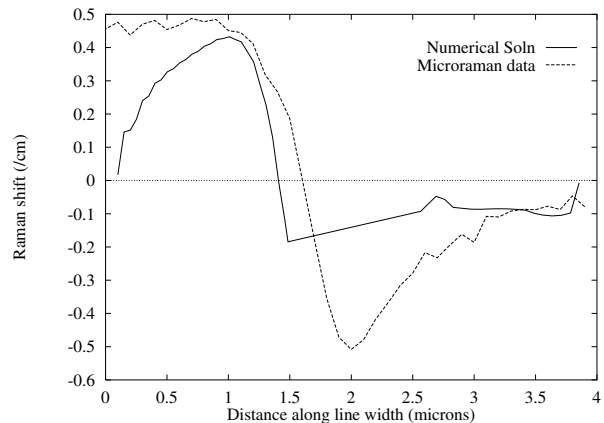


**Figure 31** : Shift in bandwidth  $\Delta\omega$  ( $\text{cm}^{-1}$ ) at the end of liner oxidation

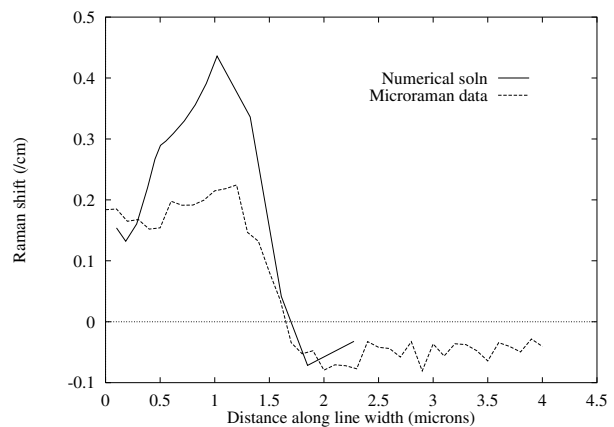


**Figure 32** : Shift in bandwidth  $\Delta\omega$  ( $\text{cm}^{-1}$ ) at the end of gate oxidation

wires, quantum dots, and substrates in Si technology. *J. Applied Physics*, vol. 79, no. 11, pp. 8145–8165.

**Johan, Z.; Hughes, T. J. R.; Shakib, F.** (1991): A globally convergent matrix-free algorithm for implicit time-marching schemes arising in finite element analysis in fluids. *Comp. Methods in Applied Mech. Engrg.*, vol. 87, pp. 281–304.

**Kao, D.-B.** (1986): *Two Dimensional Oxidation Effects in Silicon – Experiments and Theory*. PhD thesis, Stanford University, 1986.

**LeVeque, R.** (1992): *Numerical Methods for Conservation Laws*. Birkhäuser Verlag, Basel.

**Lubliner, J.** (1990): *Plasticity Theory*. MacMillan.

**Malvern, L.** (1969): *Introduction to the Mechanics of a Continuous Medium*. Prentice Hall Inc.

**Marsden, J.; Hughes, T. J. R.** (1994): *Mathematical Foundations of Elasticity*. Dover, New York.

- Navi, M.; Dunham, S.** (1997): Viscous compressible model for stress generation/relaxation in SiO<sub>2</sub>. *J. of the Electrochemical Society*, vol. 144, no. 1, pp. 367–371.
- Needs, M.; Jovic, V.; Taylor, C.; Board, K.; Cooke, M.** (1986): A 2d linear elastic model for the local oxidation of silicon using the boundary element method. In *Proceedings of the 2nd Conference on Simulation of Semiconductor Devices and Processes*, pg. 412.
- Ogden, R.** (1984): *Non-linear Elastic Deformations*. Ellis Harwood Ltd.
- Peng, J.; Chidambarrao, D.; Srinivasan, G.** (1991): Novel. A nonlinear viscoelastic model for thermal oxidation of silicon. *COMPEL*, vol. 10, no. 4, pp. 341–353.
- Pilling, N.; Bedworth, R.** (1923): *J. Instt. Metallurgy*, vol. 29, pp. 529–530.
- Rafferty, C.** (1989): Stress effects in silicon oxidation-simulation and experiments. *Ph.D. Thesis, Stanford University*.
- Rao, V. S.; Hughes, T. J. R.** (1999): On modeling thermal oxidation of silicon — Part I, Formulation. *to appear in Int. J. Numer. Methods Engrg.*
- Rao, V. S.; Hughes, T. J. R.; Garikipati, K.** (1999): On modeling thermal oxidation of silicon — Part II, Numerical Aspects. *to appear in Int. J. Numer. Methods Engrg.*
- Rekhson, S. R.** (1986): Viscoelastic relaxation. In Uhlmann, D.; Kreidl, N. J.(Eds): *Glass-Science and Technology; v. 3, Viscosity and Relaxation*. Academic Press, New York.
- Rueda, H.; Cea, S.; Law, M.** (1997): Mechanical stress modeling for silicon fabrication processes. In *International Conference on Simulation of Semiconductor Processes and Devices, SISPAD, IEEE, Piscataway, NJ, USA*, pp. 53–56.
- Senez, V.; Collard, D.; Ferreira, P.; Baccus, B.** (1996): Two-dimensional simulation of local oxidation of silicon: Calibrated viscoelastic flow analysis. *IEEE Trans. Electron Dev.*, vol. 43, no. 8, pp. 720–730.
- Sethian, J.** (1996): *Level Set Methods*. Cambridge University Press.
- Simo, J.** (1985): On a fully three-dimensional finite strain viscoelastic damage model: Formulation and computational aspects. *Comp. Methods in Applied Mech. Engrg.*, vol. 60, pp. 153–173.
- Simo, J.; Armero, F.** (1992): Geometrically nonlinear enhanced mixed finite element methods and the method of incompatible modes. *Int. J. Numer. Methods Engrg.*, vol. 33, pp. 1413–1449.
- Simo, J.; Armero, F.; Taylor, R.** (1993): Improved versions of assumed enhanced strain tri-linear elements for 3d finite deformation problems. *Comp. Methods in Applied Mech. Engrg.*, vol. 110, pp. 359–386.
- Simo, J.; Hughes, T.** (1998): *Computational Inelasticity*. Springer, New York.
- Simo, J.; Rifai, M.** (1990): A class of mixed assumed strain methods and the method of incompatible modes. *Int. J. Numer. Methods Engrg.*, vol. 29, pp. 1595–1638.
- Smeys, P.; Griffin, P.; Rek, Z.; deWolf, I.; Saraswat, K.** (1999): Influence of process-induced stress on device characteristics and its impact on scaled device performance. submitted to *IEEE Trans. Electron. Dev.*, 1999.
- Smeys, P.; Griffin, P.; Saraswat, K.** (1995): Material properties of low pressure chemical vapor deposited silicon nitride for modeling and calibrating the simulation of advanced isolation structures. *J. App. Phy.*, vol. 78, no. 4, pp. 2837–2842.
- Stademüller, M.** (1992): Mechanical stress of cvd dielectrics. *J. Electrochem. Soc.*, vol. 139, pp. 3669–3674.
- Stanford University**, Stanford, CA. *SPEEDIE 3.0 Manual*, 1995.
- Stoney, G. G.** (1909): The tension of metallic films deposited by electrolysis. *Proc. Roy. Soc. London. Ser A*, vol. 82, pp. 172–175.
- Taniguchi, K.; Tanaka, M.; Hamaguchi, C.** (1990): Density relaxation of silicon dioxide on (100) silicon during thermal annealing. *J. Applied Physics*, vol. 67, no. 5, pp. 2195–2198.
- Technology Modeling Associates, Inc.**, Sunnyvale, CA. *TSUPREM-4 Two-Dimensional Process Simulation Program, Version 6.4, User's Manual*, 1996.
- Truesdell, C.; Noll, W.** (1965): *The Nonlinear Field Theories of Mechanics*. No. III/3 in *Handbuch der Physik*. Springer-Verlag.
- Uchida, T.; Fujinaga, M.; Kotani, N.; Kawazu, S.; Miyoshi, H.** (1996): Stable solution method for viscoelastic oxidation including stress-dependent viscosity. *Jpn. J. Applied Physics*, vol. 35, no. 8, pp. 4265–4273.
- Vermilyea, D.** (1957): On the mechanism of the oxidation of metals. *Acta Metallurgica*, vol. 5, pp. 492.
- Yu, C.; Flinn, P.; Bravman, J.** (1996): In-situ measurement of viscous flow of thermal silicon dioxide thin films at high temperature. In Warren, W.; Devine, R.; Matsumura, M.; Cristoloveanu, S.; Homma, Y.; Kanicki, J.(Eds): *Amorphous and Crystalline Insulating Thin Films*, pp. 261–266. Materials Res. Soc.

**Yu, C.; Flinn, P.; Bravman, J.** (1997): In-situ stress measurements during dry oxidation of silicon. In R.R. Keller, K.S. Krisch, J. S.; Suo, Z.(Eds): *Materials Reliability in Microelectronics VII*, pp. 95–100. Materials Res. Soc.

